Early stage of erythrocyte sedimentation rate test: Fracture of a high-volume-fraction gel

Thomas John[a], Lars Kaestner [ID][a,b], Christian Wagner [ID][a,c] and Alexis Darras [ID][a,*]

[a]Experimental Physics, Saarland University, Saarbruecken 66123, Germany
[b]Theoretical Medicine and Biosciences, Saarland University, Homburg 66421, Germany
[c]Physics and Materials Science Research Unit, University of Luxembourg, Luxembourg L-1511, Luxembourg
*To whom correspondence should be addressed: Email: alexis.charles.darras@gmail.com
Edited By: Cristina Amon

Abstract

Erythrocyte sedimentation rate (ESR) is a clinical parameter used as a nonspecific marker for inflammation, and recent studies have shown that it is linked to the collapse of the gel formed by red blood cells (RBCs) at physiological hematocrits (i.e. RBC volume fraction). Previous research has suggested that the observation of a slower initial dynamics is related to the formation of fractures in the gel. Moreover, RBC gels present specific properties due to the anisotropic shape and flexibility of the RBCs. Namely, the onset of the collapse is reached earlier and the settling velocity of the gel increases with increasing attraction between the RBCs, while the gel of spherical particles shows the opposite trend. Here, we report experimental observations of the gel structure during the onset of the collapse. We suggest an equation modeling this initial process as fracturing of the gel. We demonstrate that this equation provides a model for the motion of the interface between blood plasma and the RBC gel, along the whole time span. We also observe that the increase in the attraction between the RBCs modifies the density of fractures in the gel, which explains why the gel displays an earlier onset when the aggregation energy between the RBCs increases. Our work uncovers the detailed physical mechanism underlying the ESR and provides insights into the fracture dynamics of an RBC gel. These results can improve the accuracy of clinical measurements.

Keywords: erythrocyte sedimentation rate (ESR), gravitational collapse, soft particle gel, collective behavior, multiphase flow

---

Significance Statement

The erythrocyte sedimentation rate (ESR) is one of the most widely used nonspecific inflammation marker. The underlying physics mechanism was recently demonstrated to be the gravitational collapse of the gel formed by the erythrocytes, whose maximal velocity is not reached immediately. Here, we present microscopic observations of reorganization of the erythrocyte gel during the initial acceleration. We use these observations to build a consistent physical model of the motion of the erythrocyte gel interface over the whole time span. Our model calls for an update in the clinical protocols to introduce a lower bound in the ESR normal range. Such lower bound would allow a new clinical utilization of the ESR to detect rare diseases, such as neuroacanthocytosis syndromes.

Introduction

The erythrocyte sedimentation rate (ESR) is a blood test that measures how quickly red blood cells (RBCs) settle in a test tube, and has been used for centuries to diagnose and monitor inflammatory diseases [1–5]. It is a nonspecific test that is sensitive to increases in fibrinogen and other plasma components [6–8]. Recent research has shown that it may also be useful in detecting abnormally shaped RBCs [9–11]. Despite its widespread use, the physical mechanisms governing the ESR are not yet fully understood. It has recently been demonstrated that the cause of this sedimentation is the gravitational collapse of the percolating network, also known as gel, formed by the RBCs [12, 13]. Similar to colloidal gels, this collapse presents an initial delay, during which no or negligible sedimentation is observed [14–23]. The origin of

colloidal gel sedimentation delay is still debated; however, it is likely to be associated with gel aging and the development of cracks for fluid flow within the gel [15, 16, 18, 21, 23–25]. Surprisingly, contrary to colloidal hard sphere suspensions, an increase in attractive interactions between RBCs results in gel destabilization, leading to faster structure rearrangement and apparition of cell-depleted cracks, which collapses faster [13, 26]. This feature likely contributed to the establishment of the ESR as a medical tool, as a reduced delay and an increased collapse velocity are additive for the typical medical readout, which considers the average velocity of the interface during the first hour [1, 5, 6]. In this study, we conducted experiments at different length scales to investigate the dominant mechanism of the fracture process in RBC gels, and compare it to a theoretical model

from prior literature (27). We demonstrated that higher RBC aggregation energy results in more fractures in the gel. Moreover, we derived a new equation for the delay part of our previous model for the macroscopic interface velocity (12, 13). Therefore, the model described in the current manuscript is based on an underlying physical justification and can be applied to clinical samples without losing the details of the sedimentation onset, to which the 1-h measurement is sometimes limited (28, 29). These fundamental findings can be used to extract more rigorous parameters, independent from the donor hematocrit, from ESR measurements in clinical context (28).

Microscopic experiments

Microscopic scale observations of the fracture

We performed experiments using light sheet microscopy (Z1, Zeiss, Jena, Germany), as described in a previous methodological publication (26). This technique allows enough resolution to extract the velocity field of the RBCs in the obtained image sequences using particle image velocimetry (PIV, through PIVLab (30)), but only probes a small part of the gel close to its lateral edge. More accurately, only a depth of $\approx 100\,\mu$m on an area around $1\,mm^2$ could be observed, while the whole cylindric sample has a height around 3 cm and a diameter of 1.6 mm. The area where the PIV could reliably be performed is even smaller, since absorption and diffraction of the laser light decrease the overall intensity of the picture around 700 μm from the border of the sample. It is worth noting that raw images from the light sheet microscope also reveal a lubrication layer between the Teflon container and the sedimenting cells (see Supporting Information and Fig. S1 for more details), confirming that adhesion of RBCs on the container wall is negligible (31).

As illustrated in Fig. 1, and displayed in Movies S1 and S2, when repeating experiments with samples from the same suspension, we obtained qualitatively different behaviors of the velocity field, even though the global interface velocity is reproducible. Specifically, we noted instances where the gel fluidized within the field of view, while in other cases, it exhibited a cohesive behavior, resembling a solid translation. However, we also extracted a more global parameter by extracting the velocity of the interface of the RBC gel. In order to accomplish this, we detect the position of the interface by locating the height with the strongest vertical intensity falling edge. This is achieved by averaging the vertical intensity over a horizontal width of 250 μm at each point to ensure both robust and accurate detection of the interface position. The average velocity reached by the interface is reproducible within experimental accuracy, which implies that the macroscopic dynamics of the entire sample is reproducible. Notably, velocities significantly higher than the interface velocity are observed within the gel when the velocity field is not homogeneous (Fig. 1(A–E)). However, when a nearly solid translation of the RBC gel is observed in the field of view (Fig. 1(B–F)), the peak velocity observed in the velocity probability density function (PDF) matches the interface velocity. This suggests that the RBC gel undergoes partial fluidization from an initial streamer, as observed in numerical simulations of similar gel settling (27), but this fluidization does not spread throughout the entire sample. Consequently, the rest of the sample follows the overall compaction of the structure, which ultimately determines the surface velocity. In order to confirm and generalize these conclusions, we also performed observations at bigger scales, as described in the next sections.

Mesoscopic scale observation of the fracture

To investigate the larger scale structure of RBC gels, we utilized microscopy with infrared light transmission through thin samples. We followed a similar procedure outlined in a previous paper which used blue light (26); however, we replaced the blue LED source with a halogen lamp (Nikon, LHS-H100P-1). The emitted light was filtered by an infrared long pass filter with a cutting wavelength of 950 μm (Neewer, IR950). Using infrared light provided us with higher transmission through RBCs, revealing greater detail in the structure than the blue light, which was less sensitive to the thickness of the sample. However, since RBCs still have a higher absorption in infrared range than plasma (32–34), we still see darker areas where a significant number of RBCs are present. We previously performed this kind of imaging with blue light, to obtain a better contrast. However, the transmission through RBCs is then so low that only part of the structure homogeneity could be observed (26). The lighter parts in the observed structures are therefore depleted in RBCs, as observed for the streamers in recent numerical simulations of gel settling (27). We conducted experiments with an adjusted hematocrit of $\phi = 0.45$ and various dilutions of autologous plasma with serum. Serum can be considered as plasma without fibrinogen, as the coagulation cascade occurs prior to serum extraction. This method allowed us to dilute the fibrinogen content while retaining other plasma proteins, which effectively tunes the attractive forces between RBCs (13, 28, 35, 36). We observed significant differences in the RBC gel structure for relative concentration of plasma in the liquid phase varying from 0.7 (e.g. 0.7 mL of plasma are mixed with 0.3 mL of serum) to 1 (RBCs are suspended in pure plasma). We were able to image an area of almost 1 cm × 0.87 cm in the samples, with a total width × height × thickness of $\approx 1.7\,cm \times 7\,cm \times 150\,\mu$m. As shown in Fig. 2(A–D) and Movies S3–S6, this setup revealed that during the initial stages of the sedimentation process, the RBC gel fractures, resulting in vertically oriented streamers at various horizontal intervals. To quantify the evolution of the characteristic distance D between the streamers, we computed the position of the first nonzero maxima of the horizontal autocorrelation of the image. Those quantity shows strong fluctuation; however, after a transition time of $\asymp 4,500$ s, it shows a clear decreasing trend for all fibrinogen concentrations, see Fig. 2(E). With increasing fibrinogen concentrations, i.e. stronger RBC interactions, the distance D between the streamers decreased significantly, as shown in Fig. 2(F).

In order to make sure that the structures observed arise from the backflow of the plasma, we performed experiments where the plasma is mixed with some Percoll solution, in order to match the density of the RBCs. (For the specific donor of RBCs in Movies S7 and S8, this meant using a mixture with 67% volume of Percoll and 33% of autologous plasma. Osmolarity was adjusted to 300 mOsm by adding the required amount of NaCl to the liquid.) The percoll solution is convenient as it is a suspension of biocoated nanoparticles of silica, which also act as a depletion agent between RBCs and maintains a similar network structure (37) (see also the comparison between aggregates in plasma and Percoll in Fig. S2, for which we measured similar fractal exponents). As illustrated in the Supporting Information (Movies S7 and S8), one does not observe any streamers in these experiments. If no secondary flow is observed (Movie S7), the gel does not become heterogeneous, while if some secondary flows are observed (small bubble in Movie S7 rising from the lower left corner, big bubble in Movie S8), heterogeneity in the structure appears. However, the morphology of these possible heterogeneities is different from the one
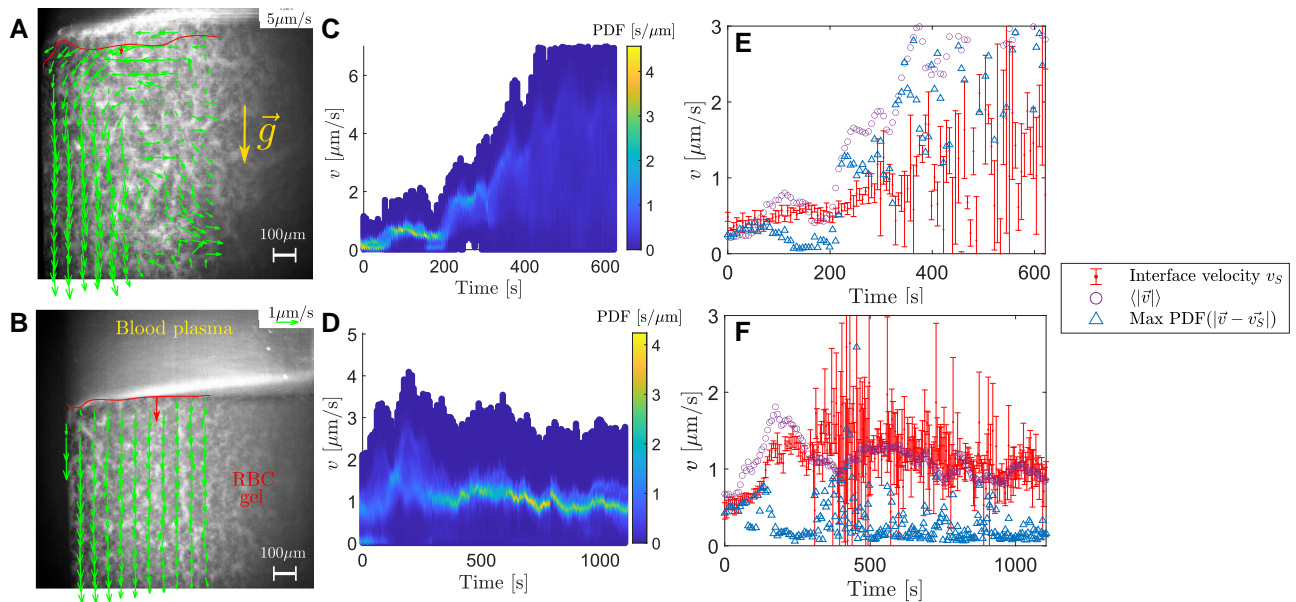
Fig. 1. Flow field characterization using light sheet microscopy. Two representative identically repeated experiments (first and second lines) are shown with samples from the same RBC suspension, locally showing qualitatively different velocity fields. A, B) Reconstructed images, with sampled velocity field at the end of the experiments (resp. ≈ 10 and 20 min). See Movies S1 and S2 for the whole characterization. C, D) Evolution of the PDF of the velocity modulus over time. E, F) Comparison of the velocity of the interface with the velocity of the flow field and its average modulus. In the upper row, the experiment displays a complex velocity field (a) due to a partial gel fluidization, which propagates from the right of the image (see Movie S1). The corresponding PDF (C) starts with a peak that gradually disappears as the network loses its integrity, while the average velocity (E) increases above the velocity of the network interface. In the lower row, the experiment exhibits a cohesive downward velocity with no significant fluidization (B, Movie S2). Instead, the gel reaches a cohesive downward velocity. The PDF D) shows a peak that persists over time and closely follows the interface velocity F). The maximal interface velocity in both experiments (E and F) is similar (around 1.3 μm/s), consistent with the maximum macroscopic interface velocity for similar samples (hematocrit $\phi = 0.45$) (12).

reported in the main article, as they are related to single event and do not possess a common preferential orientation. The areas depleted in RBCs are oriented perpendicularly to the motion of RBCs rather than parallel to their global translation in the case reported in plasma (Fig. 2).

In summary, our experimental observations demonstrated that the RBC gel is locally fluidized into streamers at the initial stage of its sedimentation, due to the backflow of plasma, in a process similar to the observations reported in simulations of the onset of colloidal gel settling (27). However, the fluidization of the structure never occurs over the whole sample. Eventually, the network of streamers stabilizes, i.e. the streamers stop forming or growing, and the RBC network undergoes a smoother reorganization, which can be described as the compression of a porous material (12).

Macroscopic scale measurements

At larger scales, one observes a motion of a sharp interface between cell-free plasma and sedimenting RBCs. The average velocity of this interface over the first hour is actually the parameter measured to perform an ESR test. This measurement is typically done by assessing the position of the interface at the beginning of the experiments and after 1 h of leaving the sample at rest. To complete our observations with macroscopic data, we conducted experiments similar to those in a previous study (13), where we manipulated the concentration of fibrinogen by mixing serum and plasma for suspensions of RBCs, with the hematocrit held constant at $\phi = 0.45$. The experimental setup is depicted in Fig. 3(A), with image analysis data presented in Fig. 3(B and C). For a further detailed explanation of the picture postprocessing, please refer to our earlier methodological publication (28).

The velocity points in Fig. 3(B) are extracted as follows. We first compute the finite difference between two successive height measurements (Fig. 3(C)), divided by the time interval of 60 s between two consecutive pictures. The resulting values are fitted by a smoothing spline. The smoothing spline is then evaluated at the time of the images to obtain the open circles in Fig. 3(B).

Modeling equations and comparison to macroscopic measurements

Equations of interface motion

In a previous manuscript by Varga et al. (27), the instability that causes the formation and spread of a fluidized portion of a settling gel, known as a "streamer," was investigated both analytically and numerically. However, their model contains several geometrical constants and parameters that are difficult to estimate experimentally. In this paper, we present an approach for simplifying their model by using only the leading terms to derive a system of differential equations that can be fitted to experimental data with just two fit parameters.

To ensure clarity, we will begin by defining the key parameters of the gel. The RBCs in the gel have a characteristic radius of $a \approx 4\,\mu m$ and experience surface attraction that is described by a potential well with a depth of U of [10 to 20] $k_B T$ and a width Δ between [10 to 100] nm (35, 38–42). For consistency, we used the approximation that $U \approx F\Delta$, where F is the characteristic disaggregation force of the cells in plasma and Δ is the potential well width. Typical measurements of disaggregation force between RBCs in plasma are between 4 and 8 pN (39). Since we considered a value of $\Delta \approx 10^{-8}$ m (40), we then obtain U to be 4×10^{-20} J to 8×10^{-20} J, i.e. 10 to 20 $k_B T$, with $T = 300$ K. The surrounding fluid has a
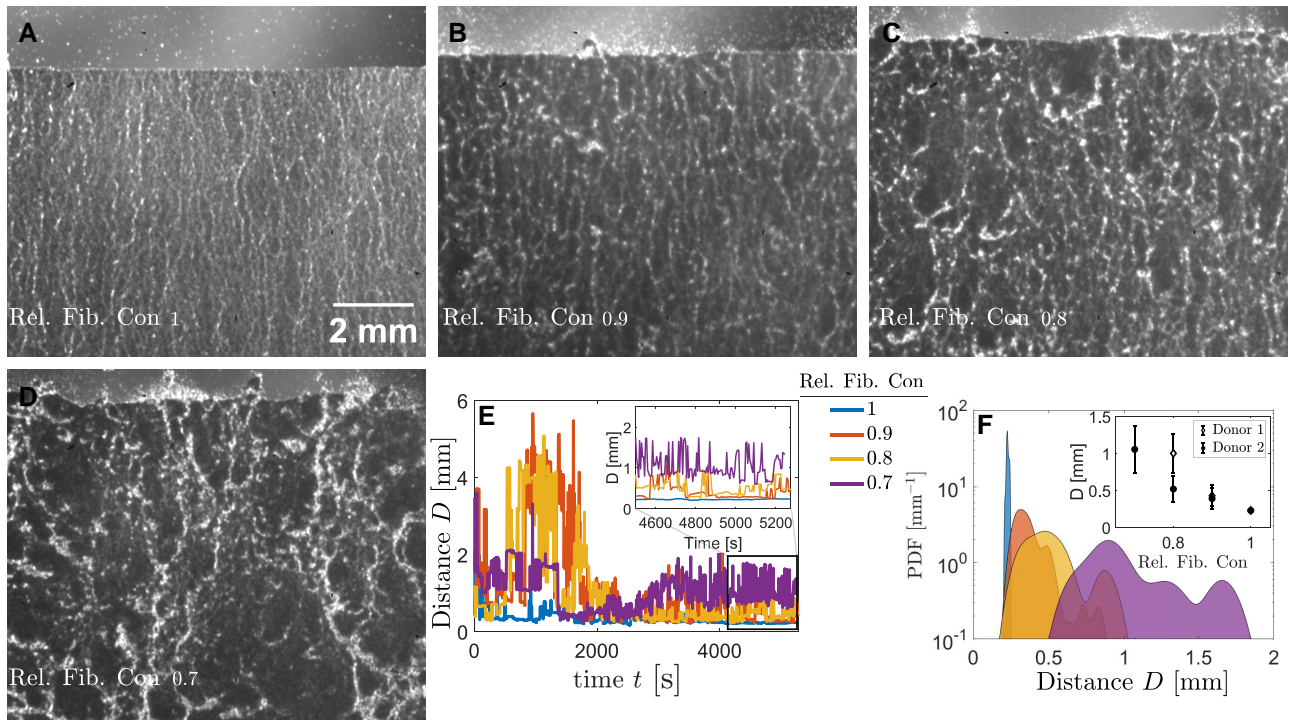
Fig. 2. Mesoscopic structures revealed by infrared light transmission through thin samples. A–D) Images captured after apparition of the streamers (i.e. after ≈ 1 h 15 min), showcasing samples with decreasing concentrations of fibrinogen from A) to D). Corresponding movies of the full experiments A)–D) are provided as Movies S3–S6, respectively. E) Time evolution of the characteristic distance between the streamers, computed as the position of the first nonzero maxima of the horizontal autocorrelation of the images. F) PDF of the first nonzero peak of the horizontal autocorrelation function, after 4,500 s (i.e. the data shown as inset in panel e). Inset shows averaged distance between the streamers plotted against the relative concentration of fibrinogen (Rel. Fib. Con.), for two different donors. As the fibrinogen concentration increases, the characteristic distance between the streamers decreases.

viscosity of $\eta \approx 10^{-3}$ Pas (43), and both the RBCs and fluid molecules have thermal energy $k_B T$. However, the density difference ρ between the cells and the fluid is 10 to $100\,\mathrm{kg/m^3}$ (44). Additionally, we will refer to the geometrical constants d_i introduced by Varga et al. (27) in their model. As defined in Varga et al. (27), those constants are unknown, independent of any physical quantity and of the order unity.

The growth of the streamer radius R over time t is determined by Eq. 2.10 in Varga et al. (27):

$$\frac{dR}{dt} = \frac{K}{\phi^{1/3}} R^{-1/3} e^{R/R^*}, \tag{1}$$

$$\text{where} \quad K = \frac{2d_1 d_2}{9} \frac{a^{1/3} U e^{-U/(d_3 k_B T)}}{\eta \Delta^2} \tag{2}$$

$$\text{and} \quad R^* = \frac{2}{d_4} \frac{k_B T}{\rho g a^2 \Delta}. \tag{3}$$

From its definition, R^* can be described as an effective gravitational length. Assuming that all dimensionless geometrical constants d_i are of the order of unity, we can estimate $K \in [10^{-11}$ to $10^{-7}]\,\mathrm{m^{4/3}/s}$ and $R^* \in [10^{-5}$ to $10^{-4}]\,\mathrm{m}$. It is worth noting that this equation is written for the case where the fractal exponent of the percolation network is approximated to $d_f \approx 2$. This assumption is supported for blood by previous literature, as discussed more in detail in the Supporting Information (section "Fractal exponent of RBCs aggregates" and Fig. S2) (13, 45–47). The simulations performed by Varga et al. also covered volume fractions up to 0.5, but potential discrepancies arising from this

parameter are discussed in the Supporting Information (section "High volume fraction").

We assume that the plasma flows mainly through the streamer, i.e. that the permeability κ of the undisturbed gel is negligible. This assumption is consistent with the fact that the initial velocity of the gel interface is below the experimental resolution. We also disregard the inverse Navier's slip length, λ, at the border of the streamers. Under these assumptions, Eq. 2.13 of Varga et al. (27) determines the average upward plasma velocity, $\langle u_f \rangle$, as $\langle u_f \rangle = K_2 R^4$, with $K_2 = \frac{\pi}{8} \frac{\rho g}{\eta D^2}$, where the distance D is assumed by Varga et al. to be equal to the cross-sectional length of the sample L. Note that this expression of K_2 is valid only if there is a single streamer, as observed in numerical simulations performed on a spatially limited system. However, we experimentally observed several streamers, as illustrated in Fig. 2(A–D). This implies that we should rather consider D to be the characteristic distance between two neighboring streamers at the interface of the gel, i.e. $D^2 = L^2/N$, with N the number of streamers which are distributed all over the cross-section area of the sample. Assuming volume conservation, the velocity of the interface can then be expressed as

$$\frac{dh}{dt} = -\langle u_f \rangle \frac{(1-\phi)}{\phi} = -K_2 R^4 \frac{(1-\phi)}{\phi}, \tag{4}$$

where the average volume fraction ϕ of the gel is dependent on both the initial volume fraction ϕ_0 and height h_0, due to volume conservation of the RBCs. Specifically, ϕ can be expressed as $\phi = \phi_0 \, h_0/h$.

Experimentally, we observed that the growth of streamer radius R is limited over time. Intermediate-scale experiments (Fig. 2, Movies S3–S6) indeed showed that the diameters of the
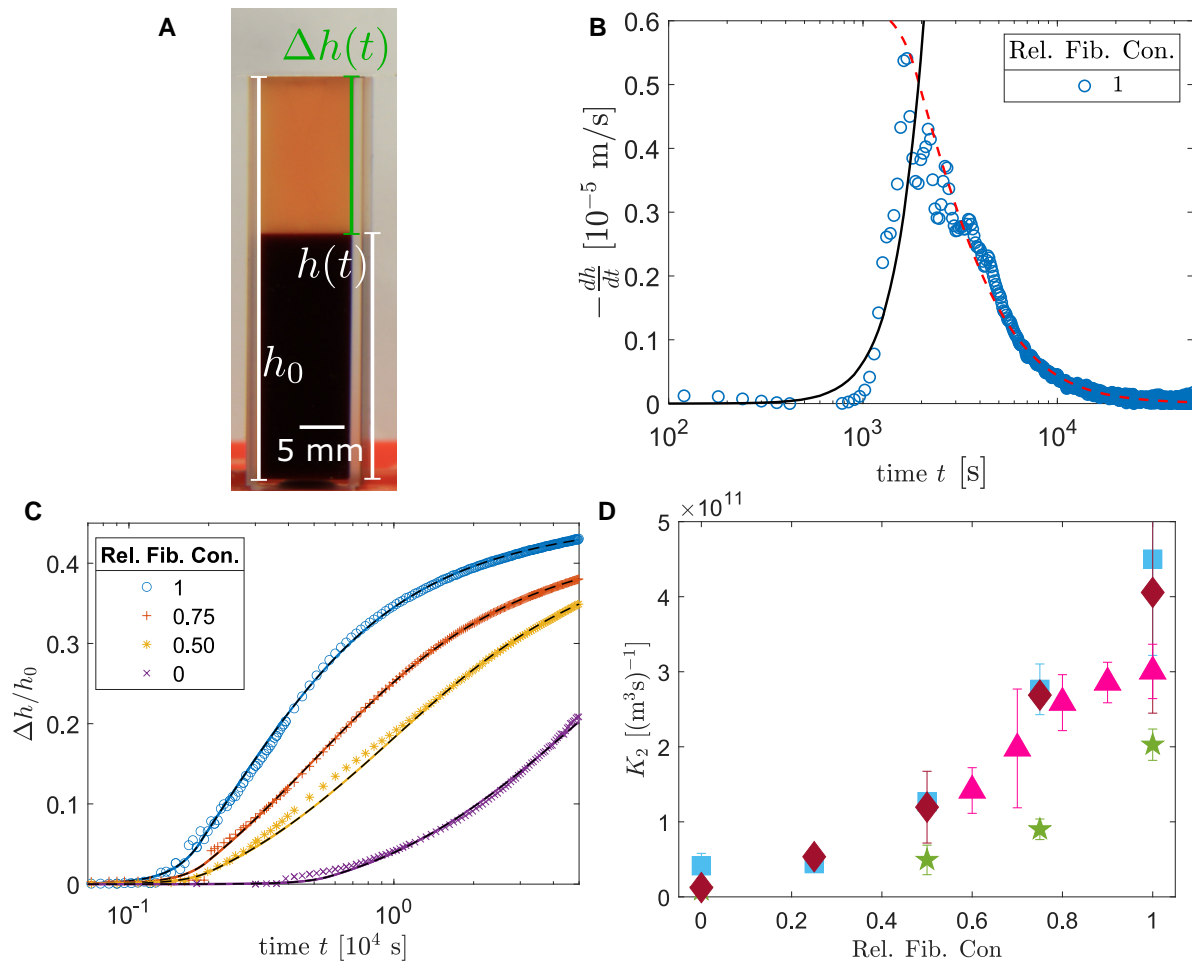
Fig. 3. Macroscopic measurements of ESR. A) Image of a cuvette used for macroscopic experiments, annotated with the measured heights. B) Velocity of the interface along time for a representative experiment. Points are data gathered from experiments, while the continuous curve is the first line of Eq. 5 (i.e. the prediction of Eqs. 1 and 4) combined and the dashed curve is the second line. Values of the fit parameters for Eq. 5 are obtained by fitting the position of the interface (panel C). C) Evolution of the RBC gel height along time. The points are measurements from image analysis, and the curves depict fits from Eq. 5. D) Evolution of the K_2 parameter from Eq. 5, as a function of the relative fibrinogen concentration. Different symbols are associated to different donors. As expected from the decreasing trend observed in Fig. 2(F) and $K_2 \propto D^{-2}$, increasing fibrinogen concentration results in an increase in K_2.

streamers saturate, and their positions stabilize. The discrepancy could be attributed to one of the assumptions made in Varga et al.'s model (27), which states that the volume fraction of particles inside the streamer is constantly similar to the bulk volume fraction. This approximation is explicitly mentioned when they assess the number of particles in a streamer, and implicitly used when they assessed the value of the flux of particles per unit area into and out of the open streamer j_{in} and j_{out} (Eqs. 2.7 and 2.8 in Varga et al. (27)). However, both their numerical simulations and our experiments demonstrate that the volume fraction within the streamers decreases. Since both fluxes are proportional to $3\phi/(4\pi a^3)$, if the volume fraction ϕ inside the streamers decreases significantly, these fluxes should therefore vanish, which explains that the streamers stabilize and the gel interface reaches a maximal velocity.

As shown by Darras et al. (12), once the maximal velocity and underlying structure of the gel are achieved, the collapse of the RBC gel can be modeled as a porous medium compressing under its own weight. The velocity of the interface is described as $dh/dt = -\frac{\rho g a^2}{\gamma \eta}\frac{(\phi_m - \phi)^3}{\phi(1-\phi)}$, where ϕ_m is the maximal volume fraction reached by the RBCs in the gel at the end of the sedimentation process, and γ is a dimensionless characteristic time of the system.

More accurately, $\gamma = \frac{\kappa_0 a^2}{A^2}$, with κ_0 the dimensionless scaling constant in the Carman–Kozeny relationship, a the characteristic size of RBCs and A is the characeristic size of the pores in the gel. In summary, the interface velocity can be expressed as

$$-\frac{dh}{dt} = \min \begin{cases} K_2 R(t)^4 \frac{(1-\phi)}{\phi} \\ \frac{\rho g a^2}{\gamma \eta}\frac{(\phi_m - \phi)^3}{\phi(1-\phi)}, \end{cases} \quad (5)$$

with $R(t)$ from Eq. 1. This equation can be fitted to macroscopic experimental data, using in total four fit parameters K, K_2, γ, and ϕ_m.

Model fitting

To numerically solve Eq. 5, an initial value $R(t=0)$ is required. However, the choice of this value has little effect on the time when dR/dt diverges as long as $R_0 \ll R^*$. This is because analytical results from Varga et al. (27) also predict a finite time divergence of dR/dt for $R(0) = 0$ (see their Eq. 2.15 and Fig. 7). Therefore, we used $R(0) = 1\mu m$, which is the same order of magnitude as the holes observed in 2D percolating networks of RBCs (13). We initially used R^* as a fit parameter, constrained in the range of

$[10^{-5}$ to $10^{-3}]$ m based on estimations from $d_4 = 1$ and $\rho \in [10$ to $100]$ kg/m^3, which led to $R^* \in [5 \times 10^{-6}$ to $5 \times 10^{-4}]$ m. However, the choice of R^* in this interval did not have a significant influence on the sum of the square residuals of the initial fits we tried. The obtained values of R^* all fell within the range of $(3.0 \pm 0.1) \times 10^{-4}$ m. Therefore, we used thereafter $R^* = 3 \times 10^{-4}$, m as a fixed parameter for all fits. As Eq. 5 is highly nonlinear, the success of the fit convergence depends on the initial guess of the other fit parameters. To simplify this problem, we first estimated the values of ϕ_m and γ through fits using the previous approximation that $h(t) = h_0$ if $t < t_0$ (13) (and therefore independent from $R(t)$, K or K_2). These estimated values of ϕ_m and γ were then used as initial guesses for the fit of Eq. 5. Additionally, we set the initial value of K_2 such that both time derivatives in Eq. 5 were equal at $R = 50\,\mu$m. This $R = 50\,\mu$m corresponds to the radius of the

depleted areas observed for the full plasma sample (Fig. 2(A), Movie S3). The parameter K is calculated through its definition in Eq. 1 with $d_1 = d_2 = 1$, $\Delta = 10^{-8}$ m, and $U = 15\,k_BT$, which yielded $K \approx 10^{-9}$ m$^{3/4}$/s as the initial guess. The fits obtained using this protocol are in good agreement with measured data, as shown in Fig. 3(B and C). The parameter K_2 exhibits a significant trend as a function of the fibrinogen concentration, as illustrated in Fig. 3(D), while the values of K are almost constant within the range of $(7 \pm 2) \times 10^{-10}$ m$^{4/3}$/s (see Fig. S4). The behaviors of γ and ϕ_m are consistent with the trends reported in Dasanna et al. (13), see also Fig. S4. As expected, due to the decrease in interdistance D between the streamers as the concentration of fibrinogen increases, we observe that $K_2 \propto D^{-2}$ increases with increasing fibrinogen concentration. This change in the geometry of the gel structure is probably related to the change in pore size that static 2D networks of RBCs exhibit when their interaction energy is modified (13). Indeed, a higher amount of bigger pores in the initial network implies more probable seeding points for the fracture of the gel. The porosity of the collapsing gel therefore increases with an increase in the fibrinogen concentration.
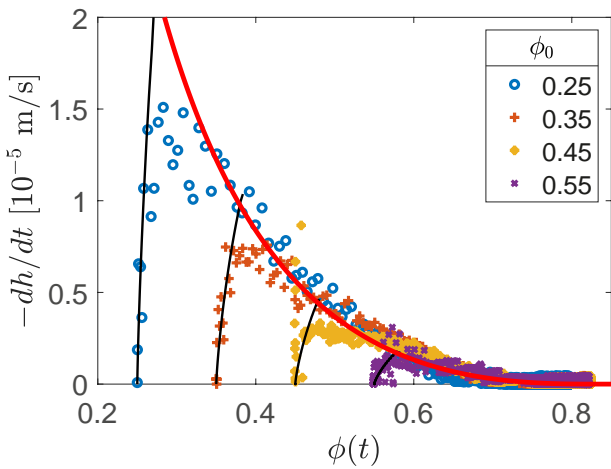
Implications for clinical ESR tests

In current medical applications, only two time-point measurements are considered to estimate the average sedimentation velocity during the first hour of the sedimentation process. Some of the current features of the standard ESR measurement are that there is no lower bound for the normal range, and no correction as a function of the sample hematocrit is universally recognized (48–51). Previous clinical studies have already highlighted that the lack of lower bound is related to the fact that the maximum velocity is often reached after the first hour, where the measurement is done (20, 29, 52). Since both time derivatives in Eq. 5 have a different dependency with ϕ, it is now clear from our model that a simple scaling of the one time-point measurement cannot be rigorously obtained. However, if one records regularly the position of the interface over a longer period of time (≈ 2 h, as already suggested in some protocols (9, 11, 20, 29)), as is now easily enabled by automation, one can extract the maximum velocity $|dh/dt|$, which scales as $|dh/dt| \propto \frac{(\phi_m - \phi)^3}{\phi(1-\phi)}$ (12). This more detailed

Fig. 4. Measurements of instantaneous sedimentation velocities for several initial volume fraction. Measurements were performed as described in a previous study, with a single donor but various initial hematocrits (9). The individual concave lines correspond to the part of the fits obtained with the first line of Eq. 5, for each sample. The common convex curve, on which all data obtained during the second phase of the sedimentation process (second line of Eq. 5) collapse, is the curve obtained with the average values of fit parameters $\gamma = 0.43$ and $\phi_m = 0.84$.
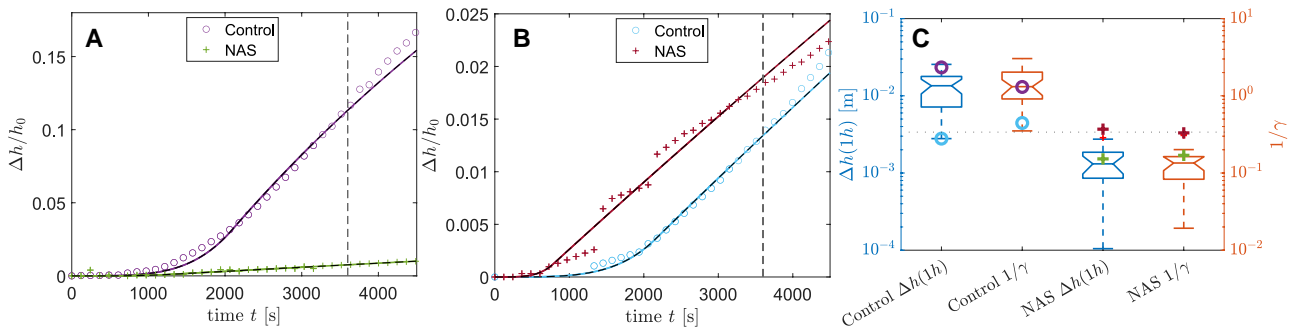

Fig. 5. Measurements of control and NAS samples. A) Example of curves obtained for NAS patient and healthy control (symbols are experimental data), along their fit of Eq. 5 (curves). This pair of curves has a behavior close to the average of their respective population. Full data have been acquired during a previous study (9). The vertical dashed line highlights the time $t = 1h$, where Δh where extracted and to which the fits were restricted. B) Extreme examples of sedimentation curves, with the highest $\Delta h(1h)$ for the patient, and the lowest $\Delta h(1h)$ for the control. One can see that the healthy control presents a long delay before reaching its maximum velocity, which is still higher than the one of the NAS curve. C) Distribution of standard ESR values obtained for the various samples after 1 h, compared to the distribution of γ values obtained for both populations, obtained by fitting the sedimentation height every minute for 1 h. A significant difference is observed in both distributions (the t-test P-value is 3.2×10^{-10} for Δh and 1.2×10^{-11} for $1/\gamma$). However, a larger difference is observed between the distributions of $1/\gamma$: the ratio of the averages is $\langle \Delta h(1h) \rangle_C / \langle \Delta h(1h) \rangle_{NAS} = 8.8$ and $\langle \gamma \rangle_{NAS} / \langle \gamma \rangle_C = 11.3$. Moreover, both populations of $\Delta h(1h)$ overlap, while even the outliers for the $1/\gamma$ distribution of the NAS samples are below the lowest value for healthy controls. The horizontal solid line is a guide for the eye.

analysis protocol could therefore provide a lower bound for the normal range of ESR, which could be used as a clinical tool to detect rare diseases, such as neuroacanthocytosis (NAS) syndromes, which presents a significantly slower ESR (9, 11). Figure 4 illustrates that the second line of Eq. 5 indeed provides a master curve on which instantaneous velocity measurements collapse, independently from the initial volume fraction. In order to illustrate the gain that such analysis would provide in clinical context, we analyzed the curves we collected in a previous study (9), comparing healthy donors and NAS syndrome patients (Fig. 5). For a fair comparison, our fits were performed only by considering data points gathered in 1 h. Not only does our γ parameter offers a measurement independent from the initial volume fraction, but it also provides a stronger difference between both sample populations (see Fig. 5(B and C)). Indeed, the ratio for average values of the traditional ESR measurement after 1 h is $\langle \Delta h(1h) \rangle_C / \langle \Delta h(1h) \rangle_{NAS} = 8.8$, while the ratio of average γ is $\langle \gamma \rangle_{NAS} / \langle \gamma \rangle_C = 11.3$. While the measurements at 1 h for the traditional ESR readout overlap across control and NAS population, the distributions of the γ parameter do not. While these data are only preliminary and further clinical results are required to confirm a substantial gain, our results and model clearly call for the establishment of a revised protocol and standard values of the ESR, including a lower value for healthy samples.

Conclusions

The experiments performed at various length scales have revealed that the initial collapse of the RBC gel is initiated by local instabilities that lead to the appearance of multiple streamers. The spatial distribution of these streamers depends on the interaction energy between the cells. This is consistent with earlier observations that higher aggregation between RBCs results in larger pore sizes, thereby increasing the possible seeding points for the emergence of streamers within the bulk. The increase in the average distance between the streamers qualitatively explains the macroscopic characteristics of the collapse: with higher cell aggregation, more streamers appear and the gel collapses sooner. On a fundamental level, these results lead to a continuous model for the gravitational collapse of a gel with a delayed onset. We have successfully connected the microscopic rearrangements of the gel structure to the macroscopic velocity of the gel interface. It is worth noting that the physical peculiarities of RBC aggregates are crucial for the aforementioned mechanisms. Indeed, the increase in sedimentation velocity with higher aggregation energy is due to the geometry of the RBC aggregates, which therefore contributes to making them a unique suspension. Understanding these peculiarities is of immense significance, particularly in clinical contexts. The present results provide a systematic approach to extract detailed parameters of the ESR, which can lead to a more rigorous and precise description of the sedimentation velocity than the current clinical standard, which only considers the average sedimentation velocity during the first hour by two time-point measurements.

Materials and methods

Blood sample collection and experiments were approved by the "Ärztekammer des Saarlandes," ethics votum 51/18, and performed after informed consent was obtained according to the Declaration of Helsinki. Blood was collected in standard Ethylenediamine tetraacetic acid (EDTA)-anticoagulated blood, as well as standard serum tubes.

Supplementary Material

Supplementary material is available at *PNAS Nexus* online.

Author Contributions

T.J., L.K., and A.D. designed the initial experimental methodology. T.J. and A.D. wrote the image analysis software and developed the formal analysis. L.K. obtained the ethical approval for the research. L.K. and C.W. acquired the core funding used for this research. A.D. was responsible for this research conceptualization, investigation, visualization, data curation, theoretical methodology, acquired secondary funding and wrote the original draft. All authors reviewed the results and edited the manuscript.

Preprints

A preprint of this article is published at https://doi.org/10.48550/arXiv.2307.02815.

Data Availability

The data underlying this article are available in Zenedo at https://doi.org/10.5281/zenodo.8006846 and can be accessed with DOI badge 10.5281/zenodo.8006846.

References

1 Bedell SE, Bush BT. 1985. Erythrocyte sedimentation rate. From folklore to facts. *Am J Med*. 78(6):1001–1009.

2 Grzybowski A, Sak J. 2011. Edmund Biernacki (1866–1911): discoverer of the erythrocyte sedimentation rate. On the 100th anniversary of his death. *Clin Dermatol*. 29(6):697–703.

3 Kushner I. 1988. The acute phase response: an overview. *Meth Enzymol*. 163:373–383.

4 Passos A, *et al.* 2022. Erythrocyte sedimentation rate measurements in a high aspect ratio microfluidic channel. *Clin Hemorheol Microcirc*. 82(4):313–322.

5 Tishkowski K, Gupta V. 2020. *Erythrocyte sedimentation rate (ESR)*. Treasure Island (FL): StatPearls Publishing.

6 Brigden ML. 1999. Clinical utility of the erythrocyte sedimentation rate. *Am Fam Physician*. 60(5):1443–1450.

7 Gray SJ, Mitchell EB, Dick GF. 1942. Effect of purified protein fractions on sedimentation rate of erythrocytes. *Proc Soc Exp Biol Med*. 51(3):403–404.

8 Greidanus NV, *et al.* 2007. Use of erythrocyte sedimentation rate and c-reactive protein level to diagnose infection before revision total knee arthroplasty: a prospective evaluation. *J Bone Joint Surg*. 89(7):1409–1416.

9   Darras A, *et al.* 2021. Acanthocyte sedimentation rate as a diagnostic biomarker for neuroacanthocytosis syndromes: experimental evidence and physical justification. *Cells*. 10(4):788.

10 Peikert K, Hermann A, Danek A. 2022. XK-associated McLeod syndrome: nonhematological manifestations and relation to VPS13A disease. *Transfus Med Hemother*. 49(1):4–12.

11 Rabe A, *et al.* 2021. The erythrocyte sedimentation rate and its relation to cell shape and rigidity of red blood cells from chorea-acanthocytosis patients in an off-label treatment with dasatinib. *Biomolecules*. 11(5):727.

12 Darras A, *et al.* 2022. Erythrocyte sedimentation: collapse of a high-volume-fraction soft-particle gel. *Phys Rev Lett*. 128(8):088101.

13 Dasanna AK, *et al.* 2022. Erythrocyte sedimentation: effect of aggregation energy on gel structure during collapse. *Phys Rev E*. 105(2):024610.

14 Allain C, Cloitre M, Wafra M. 1995. Aggregation and sedimentation in colloidal suspensions. *Phys Rev Lett*. 74(8):1478.

15 Bartlett P, Teece LJ, Faers MA. 2012. Sudden collapse of a colloidal gel. *Phys Rev E*. 85(2):021404.

16 Buscall R, *et al.* 2009. Towards rationalising collapse times for the delayed sedimentation of weakly-aggregated colloidal gels. *Soft Matter*. 5(7):1345–1349.

17 Derec C, Senis D, Talini L, Allain C. 2003. Rapid settling of a colloidal gel. *Phys Rev E*. 67(6):062401.

18 Gopalakrishnan V, Schweizer KS, Zukoski CF. 2006. Linking single particle rearrangements to delayed collapse times in transient depletion gels. *J Phys Condens Matter*. 18(50):11531.

19 Harich R, *et al.* 2016. Gravitational collapse of depletion-induced colloidal gels. *Soft Matter*. 12(19):4300–4308.

20 Hung WT, Collings AF, Low J. 1994. Erythrocyte sedimentation rate studies in whole human blood. *Phys Med Biol*. 39(11):1855.

21 Padmanabhan P, Zia R. 2018. Gravitational collapse of colloidal gels: non-equilibrium phase separation driven by osmotic pressure. *Soft Matter*. 14(17):3265–3287.

22 Poon WCK, *et al.* 1999. Delayed sedimentation of transient gels in colloid–polymer mixtures: dark-field observation, rheology and dynamic light scattering studies. *Faraday Discuss*. 112:143–154.

23 Teece LJ, *et al.* 2014. Gels under stress: the origins of delayed collapse. *Colloids Surf A*. 458:126–133.

24 Lindström SB, Kodger TE, Sprakel J, Weitz DA. 2012. Structures, stresses, and fluctuations in the delayed failure of colloidal gels. *Soft Matter*. 8(13):3657–3664.

25 Pribush A, Meyerstein D, Meyerstein N. 2010. The mechanism of erythrocyte sedimentation. Part 1: channeling in sedimenting blood. *Colloids Surf B*. 75(1):214–223.

26 Darras A, *et al.* 2022. Imaging erythrocyte sedimentation in whole blood. *Front Physiol*. 12:2292.

27 Varga Z, Hofmann JL, Swan JW. 2018. Modelling a hydrodynamic instability in freely settling colloidal gels. *J Fluid Mech*. 856:1014–1044.

28 Darras A, John T, Wagner C, Kaestner L. 2023. Erythrocyte sedimentation rate: a physics-driven characterization in a medical context. *J Vis Exp*. 193:e64502.

29 Woodland NB, Cordatos K, Hung WT, Reuben A, Holley L. 1996. Erythrocyte sedimentation in columns and the significance of ESR. *Biorheology*. 33(6):477–488.

30 Thielicke W, Sonntag R. 2021. Particle image velocimetry for MATLAB: accuracy and enhanced algorithms in PIVlab. *J Open Res Softw*. 9(1):12.

31 Mohandas N, Hochmuth RM, Spaeth EE. 1974. Adhesion of red cells to foreign surfaces in the presence of flow. *J Biomed Mater Res*. 8(2):119–136.

32 Carmona P, *et al.* 2013. Discrimination analysis of blood plasma associated with Alzheimer's disease using vibrational spectroscopy. *J Alzheimers Dis*. 34(4):911–920.

33 Meinke M, Müller G, Helfmann J, Friebel M. 2007. Optical properties of platelets and blood plasma and their influence on the optical behavior of whole blood in the visible to near infrared wavelength range. *J Biomed Opt*. 12(1):014024–014024.

34 Roggan A, Friebel M, Dörschel K, Hahn A, Mueller GJ. 1999. Optical properties of circulating human blood in the wavelength range 400–2500 nm. *J Biomed Opt*. 4(1):36–46.

35 Brust M, *et al.* 2014. The plasma protein fibrinogen stabilizes clusters of red blood cells in microcapillary flows. *Sci Rep*. 4(1):1–6.

36 Issaq HJ, Xiao Z, Veenstra TD. 2007. Serum and plasma proteomics. *Chem Rev*. 107(8):3601–3620.

37 Maurer F, *et al.* 2022. Continuous percoll gradient centrifugation of erythrocytes–explanation of cellular bands and compromised age separation. *Cells*. 11(8):1296.

38 Baskurt O, Neu B, Meiselman HJ. 2011. *Red blood cell aggregation*. Boca Raton (FL): CRC Press.

39 Lee K, *et al.* 2016. Optical tweezers study of red blood cell aggregation and disaggregation in plasma and protein solutions. *J Biomed Opt*. 21(3):035001.

40 Linss W, Pilgrim C, Feuerstein H. 1991. How thick is the glycocalyx of human erythrocytes? *Acta Histochem*. 91(1):101–104.

41 Liu Y, Liu WK. 2006. Rheology of red blood cell aggregation by computer simulation. *J Comput Phys*. 220(1):139–154.

42 Neu B, Meiselman HJ. 2002. Depletion-mediated red blood cell aggregation in polymer solutions. *Biophys J*. 83(5):2482–2490.

43 Késmárky G, Kenyeres P, Rábai M, Tóth K. 2008. Plasma viscosity: a forgotten variable. *Clin Hemorheol Microcirc*. 39(1–4):243–246.

44 Trudnowski RJ, Rico RC. 1974. Specific gravity of blood and plasma at 4 and 37 C. *Clin Chem*. 20(5):615–616.

45 Lee C, Kramer TA. 2004. Prediction of three-dimensional fractal dimensions using the two-dimensional properties of fractal aggregates. *Adv Colloid Interface Sci*. 112(1–3):49–57.

46 Lim B, Bascom PAJ, Cobbold RSC. 1997. Simulation of red blood cell aggregation in shear flow. *Biorheology*. 34(6):423–441.

47 Rapa A, Oancea S, Creanga D. 2005. Fractal dimensions in red blood cells. *Turk J Vet Anim Sci*. 29(6):1247–1253.

48 Borawski J, Myśliwiec M. 2001. The hematocrit-corrected erythrocyte sedimentation rate can be useful in diagnosing inflammation in hemodialysis patients. *Nephron*. 89(4):381–383.

49 Dintenfass L. 1974. Erythrocyte sedimentation rates: a tentative correction for haematocrit. *Rheol Acta*. 13:936–943.

50 Kim I-T, Kim J-S, Park Y-B, Lim J-S. 2004. Comparative evaluation of erythrocyte sedimentation rate by the test 1 analyzer and westergren method in patients with anemia. *Korean J Clin Lab Sci*. 36(2):137–143.

51 Kratz A, *et al.*; International Council for Standardization in Haematology (ICSH). 2017. ICSH recommendations for modified and alternate methods measuring the erythrocyte sedimentation rate. *Int J Lab Hematol*. 39(5):448–457.

52 Holley L, Woodland N, Hung WT, Cordatos K, Reuben A. 1999. Influence of fibrinogen and haematocrit on erythrocyte sedimentation kinetics. *Biorheology*. 36(4):287–297.